Metal-to-insulator transition in an Anderson insulator with Kondo impurities

Weidong Zhang* and Elliott R. Brown
Departments of Physics and Electrical Engineering, Wright State University, Dayton, Ohio 45435, USA

Richard P. Mirin
Applied Physics Division, National Institute of Standards and Technology, Boulder, Colorado 80305, USA

(Received 5 November 2021; revised 4 May 2022; accepted 3 August 2022; published 17 October 2022)

We report a voltage-controlled critical behavior observed in a GaAs epitaxial structure containing a dense array of ErAs nanoparticles. When fabricated with metal electrodes, the structure displays a voltage- and temperature-dependent metal-to-insulator transition and strong hysteresis in the current versus voltage and versus temperature characteristics, with critical temperatures as high as 77 K. Furthermore, we observed a diverging rms deviation of the electrical conductance with respect to the critical bias voltage, which further supports the existence of a phase transition. The insulating phase is governed by Efros-Shklovskii variable range hopping, and the conductance reduces beyond instrument limits as the temperature drops toward zero; supporting it is an Anderson insulator. The metallic phase displays a conductance minimum at a critical temperature behaving similarly to that of single quantum dot due to Kondo resonance, and then the conductance increases as the temperature continues to drop. Furthermore, the metallic phase displays a colossal magnetoresistance under a weak magnetic field at 77 K while the insulating phase does not. And the metal-to-insulator phase transition can be induced by the magnetic field showing a critical discontinuity, similar to that versus temperature and voltage. We propose that the metal-to-insulator phase transition can be explained by the concept of an Anderson insulator with Kondo impurities.

DOI: 10.1103/PhysRevResearch.4.043040

I. INTRODUCTION

GaAs epitaxial film with high erbium concentration (GaAs:Er) is an excellent material for ultrafast photoconductive devices due to its high dark resistivity and subpicosecond photocarrier recombination time [1–4]. When the dopant density is greater than $\sim 7 \times 10^{17}$ cm^{-3}, erbium incorporates into epitaxial film as erbium arsenide (ErAs) nanoparticles [5,6]. Because of its good lattice match with GaAs and its semimetallic nature, ErAs has been investigated as metal bases for transistors [7], and as metal contacts for single-crystal Schottky diodes [8]. In addition, several interesting properties of ErAs nanoparticle arrays have been revealed, including antiferromagnetic behavior at low temperatures [9], and low electron effective mass compared to common metals [10].

We carried out a series of growth and characterization of GaAs:Er epitaxial structures containing a significant amount of ErAs nanoparticles for the development of ultrafast photoconductive devices [11–13]. Along the way, we have observed an interesting metal-to-insulator transition (MIT) behavior. The MIT is a strong function of bias voltage, temperature, and magnetic field, displaying several orders of magnitude discontinuity and strong hysteresis. We have found it is significantly different than the well-studied MITs in structures such as Si:P or arrays of small metallic nanoparticles [14–19]. And this new MIT has not been previously reported in any studies of magnetic-impurity-doped quantum dot systems [20–25].

We propose that the insulating phase of the MIT is an Anderson insulator arising from the strong disorder of ErAs nanoparticles, and the metallic phase is due to Kondo impurities in Anderson insulators because Er is a rare-earth element.

II. EXPERIMENTS AND RESULTS

A. Samples

The rare-earth-doped epitaxial structures under test had two different erbium (Er) concentrations: (A) 3.5×10^{17} cm^{-3} for control structure (1.25 μm thick), and (B) 8×10^{20} cm^{-3} (1 μm thick) (Fig. 1). These doping levels straddle the widely accepted solubility limit of $\sim 7 \times 10^{17}$ cm^{-3} for the incorporation of atomic Er, so structure B is expected to have many ErAs nanoparticles [Fig. 2(a)], and structure A few to none.

The growth was carried out by molecular beam epitaxy (MBE) on 76.2 mm diameter semi-insulating GaAs substrates at a temperature of 600 °C as measured using band edge thermometry. The growth rate was ~0.65 monolayers per

*Also at Terapico LLC, Beavercreek, Ohio 45431, USA; wzzhang@fastmail.fm

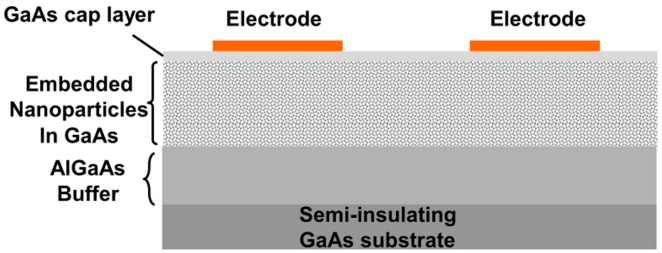

FIG. 1. Cross view of GaAs:Er epilayer.

second. The Er flux was calibrated using secondary ion mass spectroscopy on a separate structure.

The Er and As atoms spontaneously form ErAs nanoparticles because of the mismatch of the NaCl crystal lattice of ErAs with the zinc blende of GaAs, and hence the nanoparticles are energetically favored during the growth. Transmission electron microscope (TEM) images of epitaxial structure B [Fig. 2(a)] show that the GaAs remains a single crystal with embedded ErAs nanoparticles that are spherical or nearly so. No obvious stacking faults or other defects were observed in the TEM images. The dimensions of the nanoparticles in structure B are predominantly distributed in the range of ∼1–4 nm [Fig. 2(b)], the "most likely" being 1.6 nm height and 2.5 nm width. They are densely packed with a typical center-to-center separation of ∼3.4 nm and an estimated concentration of $\sim 5 \times 10^{18}$ cm^{-3}.

If perfectly spherical, a 2.0 nm diameter nanoparticle would have a potential energy profile like that illustrated in Fig. 2(c), where the Γ-point (*X*-point) levels correspond to the valence (conduction) band edges in bulk ErAs. Unlike in bulk ErAs, the Γ level lies below the *X* level due to the quantum size effect. Quantum mechanical calculations indicate that a nanoparticle may contain at least one bound energy level, and sometimes may accommodate two bound levels resonant to ∼1550 nm. This is supported by near-infrared photoabsorption data (Ref. [26], Fig. S1 of [27], and Ref. [28]), and other studies using scanning tunneling microscopy [29]. Electron occupancy of energy levels is determined by the Fermi level, which is assumed likely pinned at the midgap of GaAs by interface states [29].

To characterize each epitaxial structure, we fabricated two-terminal gap devices as illustrated in the cross-section view of Fig. 1. Two 4.5 mm wide, 5.0 mm long, ∼200 nm thick AuGe stripes were fabricated on top of the epitaxial layer separated by a gap of ≈0.5 mm. Before the deposition of metal contacts, the sample was cleaned with acetone, isopropyl alcohol, and deionized water, and then dipped into a 90:10 HCl solution for ∼30 s to get rid of native oxide. The electrodes were then annealed in a nitrogen environment at 465 °C for 30 s. This is a well-known technique for reducing contact resistance by solid-state diffusion of Ge into GaAs. After the annealing, the AuGe electrodes provide good ohmic contacts. We conducted four-terminal as well as transmission line measurements at room temperature, and the specific contact resistance was estimated to be $\sim 1 \times 10^{-6}\ \Omega\,\text{cm}^2$.

Four such devices were fabricated for this study: device A on epitaxial structure A, and three devices on structure B, labeled devices B1, B2, and B3. Device B1 displayed the

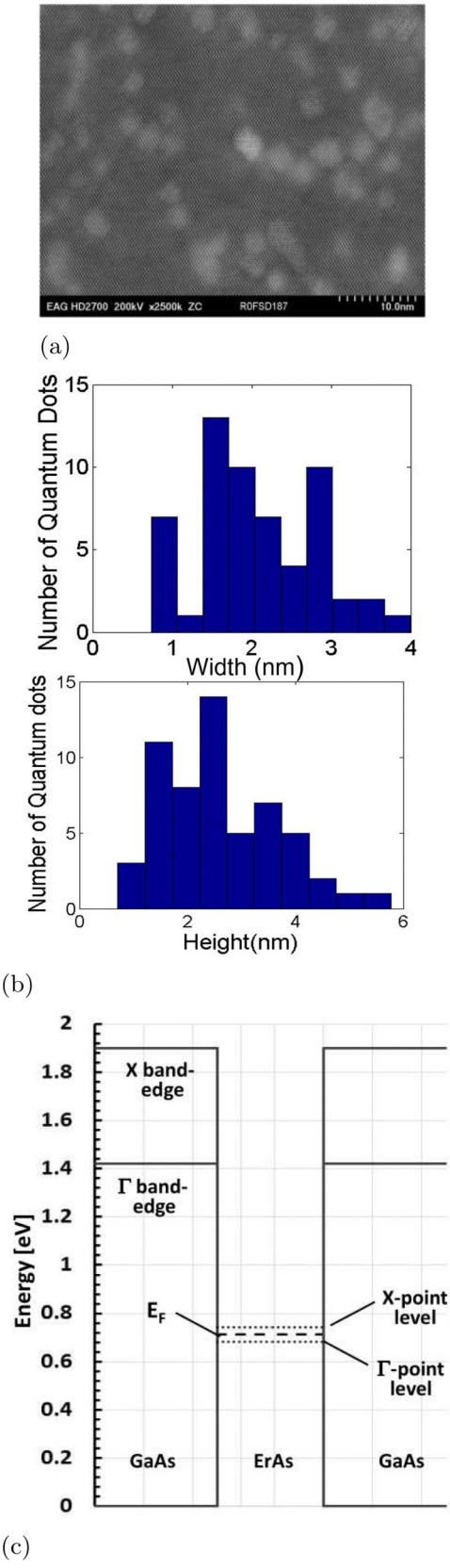

FIG. 2. (a) A cross-sectional TEM image. The light-tone disks indicate the presence of ErAs nanoparticles, consistent with Er being much heavier than Ga. (b) Histograms for nanoparticle size distributions. (c) A potential well model based on 1550 nm optical absorption and photoconductivity measurements [26].

TABLE I. Hall data for control structure A at 300 K.

Resistivity (Ω cm)	12.4
Sheet charge density ($1/cm^2$)	3.6×10^{11}
Hall mobility ($cm^2/V\,S$)	211.4
Sample polarity	*p*-type

original MIT behavior, and devices B2 and B3 were fabricated to check for reproducibility of the novel effects, and to investigate critical-point fluctuation and magnetoresistance.

B. Measurements of the control sample

The device under test (DUT) was mounted on the cold finger of a Gifford-McMahon closed-cycle He refrigerator. Apiezon grease was applied between the DUT and the cold finger to ensure good thermal conduction. Before the DUT was mounted, it was cleaned with acetone and isopropyl alcohol. The temperature was measured with a calibrated silicon diode and read with a temperature controller. All currents were measured with a source meter, which had a minimum range limit of 1 pA. The source meter was precise to measure resistance as low as 100 Ω and as high as 200 MΩ. A Python script was programmed to record the reading of the temperature controller and the source meter automatically. All measurements were conducted in a dark environment to eliminate photogeneration.

To qualify our experimental technique, we started with device A—the control sample—and measured current (I) versus temperature (T) at different bias voltages (V_b) with low source impedance (V mode) (Table I). The behaviors in Figs. 3 and 5(a) show typical conduction mechanisms for semiconductors doped with point defects. Specifically, at 45 V bias and between ∼130 and 300 K, the conductance ($G = I/V_b$) displays an Arrhenius behavior with activation energy of ∼0.13 eV [Fig. 4(a); Table II]. As the temperature drops from ∼130 to ∼95 K, the G vs T curve is fitted with Mott variable range hopping (VRH) [Fig. 4(b)] [30]; below ∼95 K but above the "freeze-out" temperature ∼53 K, G vs T is best fitted with Efros-Shklovskii (ES) VRH [Fig. 4(c)] [31]. Below ∼53 K, the current drops monotonically, such that to the lower limit of the source meter, so to the best of our capabilities, it is insulating. Analysis of the 5 V bias curve yields similar results, but without the ES VRH at low temperatures [Figs. 5(b) and 5(c)]. The Arrhenius fitting for the range of ∼193–300 K yields an activation energy of ∼0.18 eV, which is higher than that of the higher bias $V_b = 45$ V [Fig. 4(a)]. The "freeze-out" temperature is ∼71, K, higher than the G vs T curve for $V_b = 45$ V [Fig. 5(c)]. Furthermore, we did I-V sweeps at lower temperatures such as ∼5.8 K. The current in the range of 0–140 V was unmeasurable with the source meter, thus consistent with the insulating behavior.

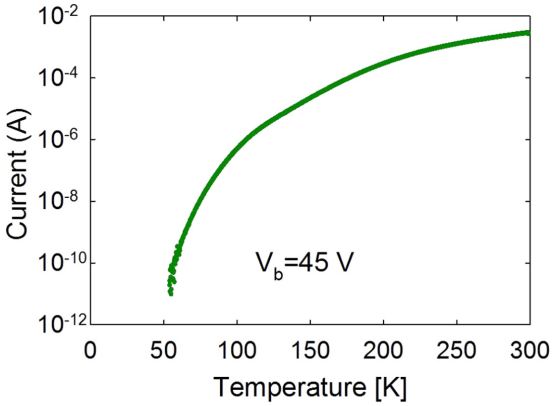

FIG. 3. Device A (the control structure). Current versus temperature when bias was 45 V.

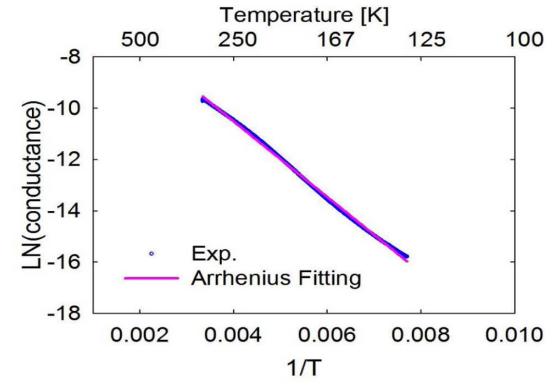

(a)

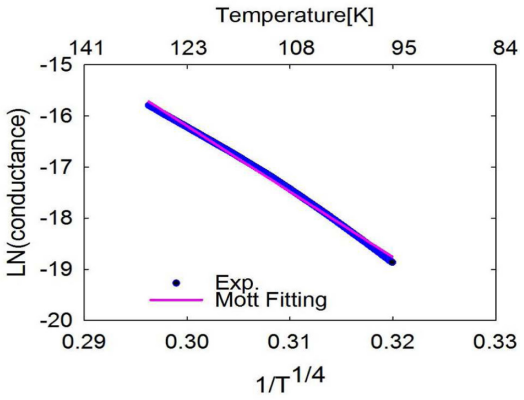

(b)

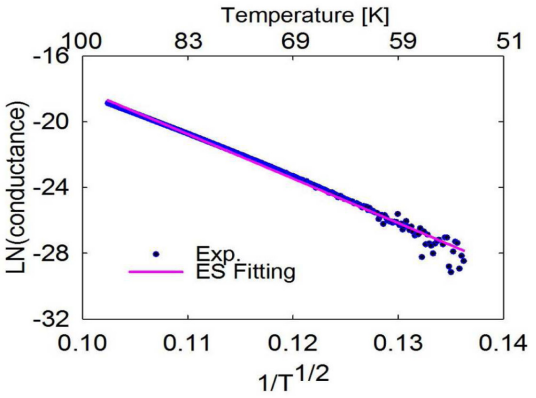

(c)

FIG. 4. Device A (the control structure). (a) Arrhenius fitting of Fig. 3 for the range of T ∼ 130–300 K. (b) Mott-type VRH fitting of Fig. 3 for the range of T ∼ 95–130 K. (c) ES-type VRH fitting of Fig. 3 for the range of T ∼ 53–95 K.

TABLE II. Fitting parameters for device A.

Transport	Fitting parameters	Bias 45 V	Bias 5 V
Arrhenius fitting [ln (G) vs $1/T$]	Temperature range (K)	130–300	193–300
	Fitting equation	$y = -4.6 - 1474.5x$	$y = -4.7 - 2110.7x$
	R^2 of the fitting	0.9987	0.9970
Mott fitting [ln (G) vs $1/T^{1/4}$]	Temperature range (K)	95–130	71–193
	Fitting equation	$y = 22.2 - 128.0x$	$y = 17.9 - 123.8x$
	R^2 of the fitting	0.9973	0.9902
ES fitting [ln (G) vs $1/T^{1/2}$]	Temperature range (K)	53–95	N/A
	Fitting equation	$y = 9.0 - 270.3x$	N/A
	R^2 of the fitting	0.9933	N/A

C. Voltage-driven insulator-to-metal transition and conductance minimum

Next, we characterized the device labeled as B1 for structure B with the known high concentration of ErAs nanoparticles, $\sim 5 \times 10^{18}$ cm^{-3}. Figure 6 displays the low-bias I-V curve at room temperature, which shows a linear relationship—direct evidence that the electrode contacts are ohmic, not Schottky. Figure 7(a) plots the I vs T curve in V mode $V_b = 5$ V (similar to the 10 V bias data presented in Figs. S2 and S3 of [27]). Unlike the piecewise conduction mechanisms found for device A, the entire conductance curve between ~17 and 300 K is fitted better by ES VRH [Fig. 7(b); Table III] than Mott VRH (Fig. S4 of [27]), and there is no crossover to either Mott-type or Arrhenius behavior at the high temperatures. Lacking Arrhenius activation is consistent with the fact that the Fermi level is positioned near the midgap of GaAs, too deep to be thermally excited. This ES-type behavior is commonly seen in nanoparticle arrays or quantum-dot systems [32], and it also suggests that the hopping conduction is dominated by electron-electron interaction. The localized density of states has a soft "Coulomb gap" centered around its Fermi level and is likely proportional to $(E - E_F)^2$ [33]. The existence of this type of Coulomb gap has previously been demonstrated with scanning tunneling microscopy results [29]. As T drops below ~17 K, the current decreases to the lower limit of the source meter, and the precipitous drop is consistent with the insulating behavior expected from the Coulomb gap. Both the temperature-decreasing and -increasing curves [Fig. 7(a)] are practically superimposed over the entire range, contrary to the hysteretic behavior described next.

Figure 8(a) shows I vs T behavior in V mode when device B1 was biased at a higher voltage of $V_b = 45$ V with the other experimental conditions kept the same (similar to the 50 V bias curve displayed in Fig. S5 of [27]). On the temperature-decreasing curve, a conductance (or current) minimum occurs at a critical temperature of $T_C \sim 16.3$ K, below which the current suddenly jumps up almost two orders of magnitude to $\sim 5.3 \times 10^{-6}$ A and then tends to increase slightly, down to at least 4.2 K [Fig. 8(b)]. This finite zero-temperature conductance is a metallic behavior [34]. On the temperature-increasing curve, which forms a clockwise hysteresis with the decreasing curve, the high conductance ($G = I/V_b$) is approximately constant up to $T_K \sim 49$ K, where a steep decrease occurs [magnified in Fig. 8(c)]. However, the drop is not as abrupt as for the temperature-decreasing curve near T_C.

Next, I-V curves were taken for device B1 in V mode at a fixed temperature below T_C, namely $T \approx 4.3$ K. The voltage was swept from low to high and then high to low, yielding the counterclockwise hysteresis loop shown in Fig. 9(a). When V_b is less than $V_L \approx 16$ V, the device is insulating with unmeasurable current. As V increases, the current I increases monotonically but then displays a sudden increase in slope at an intermediate voltage $V_I \approx 35$ V. In the range of V_L to V_I, we found that the I-V characteristic was fitted with a power law having an exponent of $k \approx 4.8$, i.e., $I \approx (V_b - V_C)^k$, where V_C is threshold voltage [Fig. 9(b); Table IV], which may originate from the disorder in nanoparticles [19].

This type of hopping conduction behavior has previously been studied in nanoparticle arrays or quantum-dot assemblies, suggesting that transport through a small number of nanoparticles at a time is determined by cooperative electronic behavior via multiple inelastic co-tunneling [32]. The average number of nanoparticles involved in the process at this temperature is estimated from the exponent $N \approx (k + 3)/2 \sim 4$. This agrees with Ref. [32] that a typical co-tunneling involves 4–4.5 "grains" at low temperatures. As temperature rises, the power law still holds, but k decreases and eventually becomes $k \approx 1$ at room temperature (Fig. 6).

Further, at a higher voltage of $V_H \approx 51.5$ V, critical behavior is again observed as the current abruptly jumps from 4.4×10^{-8} to 8.0×10^{-6} A—over two orders of magnitude. The abrupt increase, which is consistent with the temperature-dependent curves at fixed bias such as 45 V [Fig. 8(a)], is not likely cross-gap impact ionization in GaAs, or that of nanoparticles as the electric field in our experiments is too low, <103 V/cm, compared to the typical threshold field (>1×10^5 V/cm) in bulk GaAs. This type of temperature dependence has not been observed in any other nanoparticle arrays even under high bias voltage, that is, beyond the Coulomb blockade regime [32].

As V_b sweeps down, I drops rapidly at a (lower) voltage of ~26.3 V. Furthermore, as T is increased from 4.4 to 5.8 K, V_H (V_L) of the current-voltage curves shifts to the right (left) by ~1 V, respectively [Fig. 9(c)].

D. Current fluctuation measurements

Next, we studied electrical fluctuation of device B1 in V mode around the critical voltage using a bias-tee circuit. The

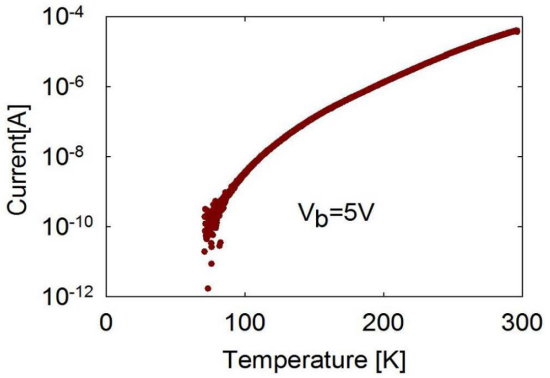

(a)

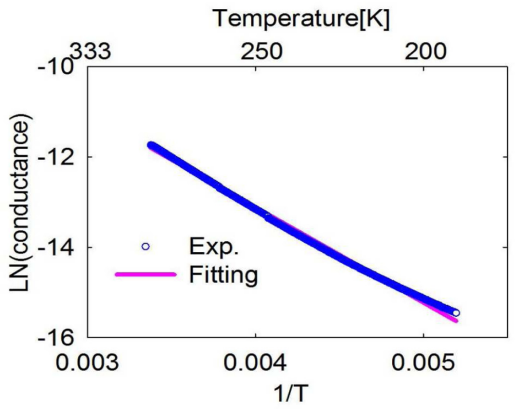

(b)

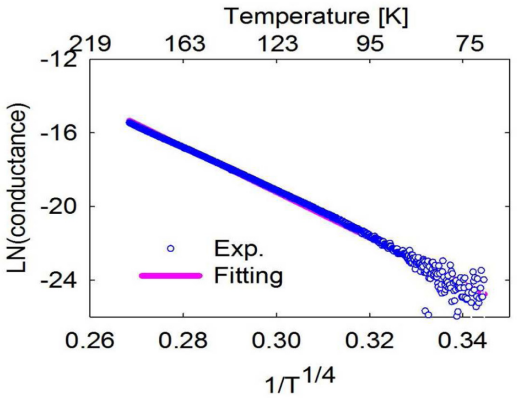

(c)

FIG. 5. Device A. (a) Current versus temperature at bias 5 V. (b) Arrhenius fitting of (a) for the range of $T \sim 193$–300 K. (c) Mott-type VRH fitting of (a) for the range of $T \sim 71$–193 K.

bias tee had a rise time of 45 ps and a bandwidth from 3.5 kHz up to 7 GHz. Its inductance was 1.34 mH, and capacitance was 0.9 μF. The DUT was connected to the RF/DC port of the bias tee. The source meter was connected to the DC port, which supplied the bias voltage to the DUT. The wave form was measured with an oscilloscope connected to the RF port. The input port of the oscilloscope was set to AC coupled with a 1 MΩ input resistance. The bias tee directed most of spectral power to the oscilloscope. Therefore, the fluctuation of the current $\delta I(t) \approx \delta V(t)G$ is proportional to the fluctuation of

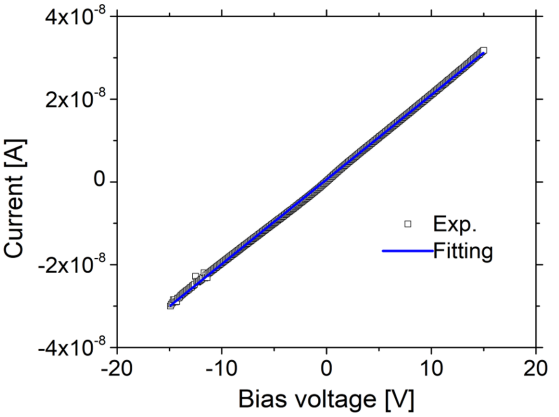

FIG. 6. I-T behaviors for device B1. Linear I-V curve at 300 K.

the voltage $\delta V(t)$ measured with the oscilloscope, where G is the differential conductance of the DUT, which can be estimated from the I-V curve.

The time series of $\delta V(t)$ were taken for V_b biased below and above the threshold V_H, respectively [Fig. 10(a)]. The $\delta I(t)$ increased (decreased) as the bias voltage approached (departed from) the critical V_C, resulting in a singular behavior shown in Fig. 10(b). The largest measured deviation is at 53 V, which is closest to the critical bias $V_H \sim 51.5$ V [Fig. 9(a)]. Divergent fluctuations at the critical point are universal in nature of all

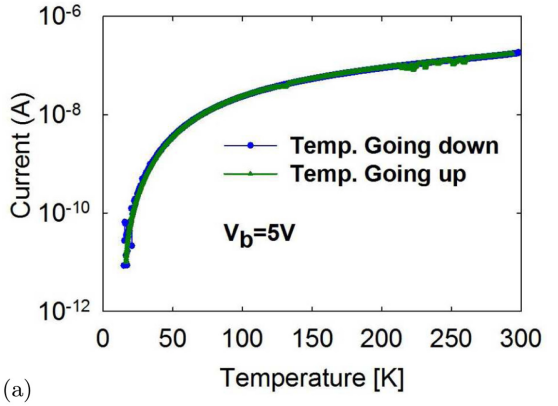

(a)

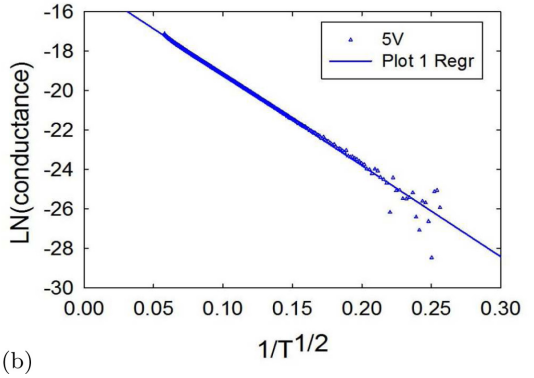

(b)

FIG. 7. I-T behaviors for device B1. (a) Current versus temperature curve at bias 5 V. (b) Fitting of (a) with Efros-Shklovskii VRH.

TABLE III. Fitting parameters for device B1.

Transport	Fitting parameters	Bias 45 V	Bias 5 V
ES fitting [ln (G) vs $1/T^{1/2}$]	Temperature range (K)	N/A	17–300
	Fitting equation	N/A	$y = -10.0 - 29.6x$
	R^2 of the fitting	N/A	0.9849
I vs ln (T/T_K)	Temperature range (K)	40–49.7	N/A
	Fitting equation	$y = -3.4 \times 10^{-7} - 5 \times 10^{-5} \ln(T/T_K)$	N/A
	R^2 of the fitting	0.8946	N/A

phase transitions [35–37]. Thus Fig. 10 supports the existence of an MIT phase transition in the epitaxial structure B.

E. Reproducibility measurements

To investigate the reproducibility of the results for device B1, we fabricated a second sample on epitaxial structure B, labeled device B2. It was on a chip from a different spot of the structure-B wafer.

At a low fixed bias $V_b = 10$ V, it exhibits a rapidly decreasing conductivity as the temperatures drop below ∼66 K [Fig. 11(a)]. At a high bias such as $V_b = 50$ V, the current (or conductance $G = I/V_b$) for both the increasing and decreasing curves first drops to a minimum at $T_C \sim 21.9$ K and then increases as the temperature approaches lower values [Fig. 11(b)]. The curves correspond to a clockwise hysteresis loop between the two temperatures $T_C \sim 21.9$ K and $T_K \sim 44.9$ K. The current increase at T_C is abrupt but the drop at T_K is more gradual. The current achieves a minimum at T_C and continues to increase with decreasing temperatures below T_C, behaving like a metal.

When set at a fixed temperature such as $T \sim 6.3$ K, the I-V sweep in both forward and reverse directions displays a six-order-of-magnitude discontinuity, and the two curves comprise a counterclockwise hysteresis loop [Fig. 11(c)], similar to the behavior of device B1. It is not exactly the same, probably because of the nonuniformity distribution of nanoparticles.

F. Colossal magnetoresistance

To investigate the magnetoresistance effect, we fabricated a third device based upon structure B, device B3, which had the same strip electrodes as the other devices, but on a smaller chip that could fit in a small liquid-nitrogen Dewar in the bore of an electromagnet.

The measured I-V curves are plotted in Fig. 12(a) at a fixed temperature of 77 K for both V-mode and I-mode (high source impedance) bias. As expected, Fig. 12(a) shows two discontinuities in current at the critical values of the increasing- and decreasing-voltage curves. And the discontinuity voltages are $V_H \approx 35.8$ and $V_L \approx 32.3$ V, respectively. The I-V characteristic for lower biases below V_H was well fitted with the power law $I \approx (V_b - V_C)^k$, in which the exponent is $k \sim 4.6$ [Fig. 12(b); Table IV]. This again supports that the conduction is via macroscopic co-tunneling among nanoparticles. It is a precursor of the current discontinuities. Figure 12(c) shows a voltage discontinuity at a critical value (≈40.0 μA) of the increasing current curve. We also notice that the curves in Fig. 12(c) are noisier than those of Fig. 12(a) during the transition. We attribute this to the fact that I-mode bias allows access to the inherently unstable region of the I-V curve laden with critical-point fluctuations. The rest of the curve becomes "quieter" just below and above the critical transition.

Finally, we utilized the smaller size of the device B3 chip to measure magnetoresistance at $T = 77$ K. A uniform, tunable magnetic field was applied perpendicular to both the current direction and the device-B3 substrate forming the so-called Voigt configuration.

When device B3 was biased into the insulating phase at a bias of $V_b = 10$ V, the magnetoresistance changes little in response to the magnetic field [Fig. 13(a)].

But when it was in the metallic phase at a bias of $V_b = 39$ V, the magnetoresistance is positive, and becomes so large that the ratio [defined as $[R(B) - R(0)]/R(0)$] reaches values of ∼1627% at ∼947 G [Fig. 13(b)]. This magnitude of magnetoresistance is comparable to that first reported for GaAs:ErAs systems at a much lower temperature of 1.5 K, which was attributed to a magnetic polaron effect [21].

On both the B-field-increasing and -decreasing curves, there is a sudden jump at $B \approx 350$ G. This is similar to the voltage- and temperature-induced discontinuities described earlier for devices B1 and B2. Above $B \sim 408$ G, the magnetoresistance resumes to a slower rate of increase with magnetic field, approaching an asymptote which is almost the same as the level of insulating state prior to the MIT transition. Therefore, the experimental data suggest that the insulating phase transforms into the metallic phase at a critical B_C of ≈350 G.

III. DISCUSSION

Temperature, voltage, and magnetic characteristics, specifically the colossal magnetoresistance effect (CMR), displayed during the metal-to-insulator transition, have been seen in the several MITs of strongly correlated materials, such as transition metal compounds [38] (e.g., EuO), or perovskite manganites [39–42] (e.g., $Pr_{1-x}Ca_xMnO_3$ and $La_{5/8-x}Pr_xGa_{3/8}MnO_3$). The similarity should provide clues for understanding the experimental data presented in this paper.

For example, the CMR measured in this investigation (≈16 times) is significantly smaller than the one measured in $Pr_{1-x}Ca_xMnO_3$, which is on the order of 10^5, but at a much stronger magnetic field $B \approx 6.8$ T [40]. Moreover, the CMR in $Pr_{1-x}Ca_xMnO_3$ is negative and is believed to be related to the ferromagnetic metallic state. The CMR in sample B3 (of

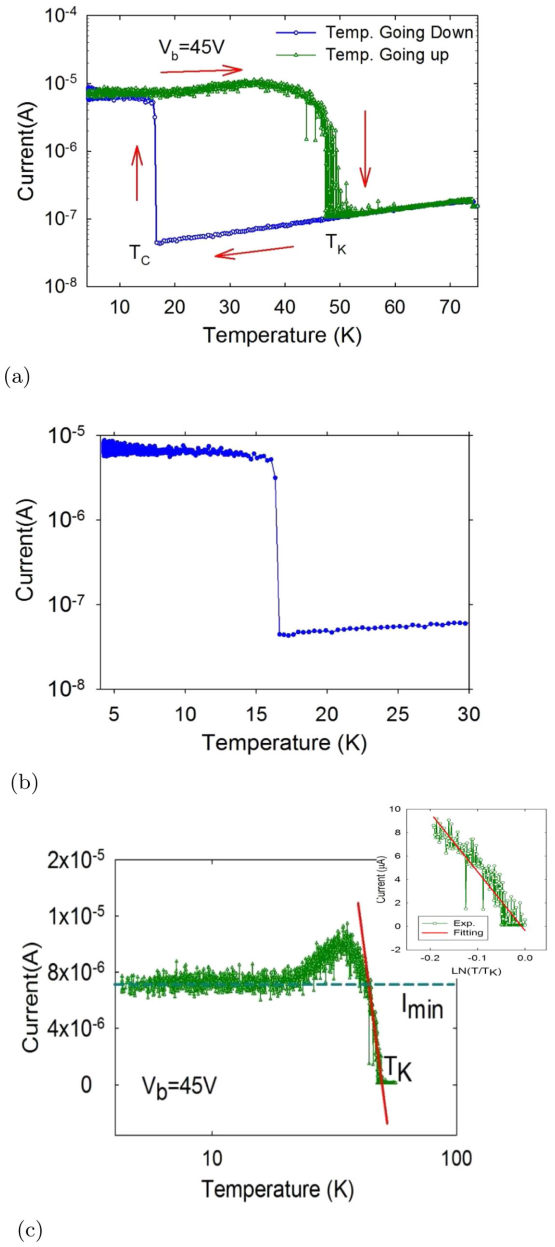

FIG. 8. I-T behaviors for device B1. (a) Current versus temperature when the bias was 45 V. On the temperature-decreasing curve, at $T_C \sim 16.3$ K, the current jumps up about two orders of magnitude, and then increases slightly as the temperature decreases toward zero. On the temperature-increasing curve, the high conduction is maintained above T_C, yielding a strong hysteresis. The upper limit of the hysteresis occurs at $T_K \sim 49$ K. (b) Zoom-in on the temperature-decreasing curve of (a). (c) By isolating the temperature-increasing curve of (a), the conductance is fitted with $|\ln(T/T_K)|$ (red line). The fitting curve is plotted on the right side of (c) (Table III).

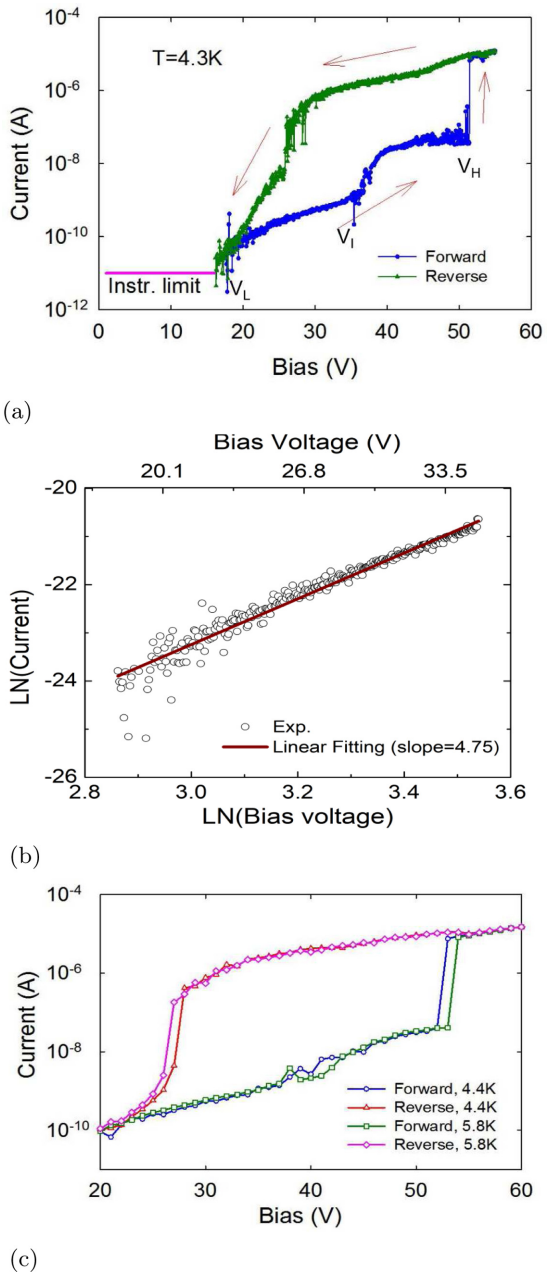

FIG. 9. Device B1. (a) Current versus bias voltage sweeps for device B1 in both forward and reverse directions at $T = 4.3$ K. The curves display a pronounced hysteresis loop—a telltale sign of phase transitions. (b) $\ln I$ vs $\ln V_b$ fitting in the range V_L and V_I on the forward-sweeping curve of (a) (Table III). (c) Current versus bias voltage sweeps for device B1 at $T = 4.4$ K and 5.8 K. V_H is shifted to the right by $\sim$1 V while V_L is shifted to the left by $\sim$1 V as T varies from 4.4 K to 5.8 K, respectively.

this research) is positive, and thus the metallic phase cannot be related to any ferromagnetic state.

A. The insulating phase

First, the possibility of surface leakage current is eliminated as it would not display the power-law I-V characteristic shown in either Figs. 9(b) or 12(b). Generally, the Fermi level for GaAs is pinned near the midgap of the semiconductor because of the large density of surface states contributed by As and Ga antisite defects. These states are deprived of electrons due to the band bending caused by the Fermi-level pinning. This would lead to an increase in resistivity with decrease in temperature, not the decreasing resistivity measured in our samples.

TABLE IV. Power-law fitting for devices B1 and B3.

Power law	Fitting parameters	Temperature (K) B1 at 4.3 K
ln (I) vs ln (V)	Voltage range (V) Fitting equation R^2 of the fitting	16–35 $y = -37.5 + 4.8x$ 0.95513
		B3 at 77 K
ln (I) vs ln (V)	Voltage range (V) Fitting equation R^2 of the fitting	0–35.8 $y = -25.9 + 4.6x$ 0.9802

Further, as shown in Fig. 6, the AuGe contact is ohmic. As shown in Figs. 7(a) and 7(b), the fitting of the conductance versus temperature curve is consistent with ES variable range hopping, a major conduction mechanism of noncrystalline solids. Furthermore, as shown in Figs. 9(b) and 12(b), the power law of the I-V curves, $I \approx (V_b - V_C)^k$, is consistent with macroscopic co-tunneling, a unique transport mechanism for quantum dot/nanoparticle/grain systems. These facts support that the transport mechanisms are from the samples themselves, not dictated by any effects from Schottky contacts.

Thus the experimental data in Fig. 7 and the TEM image in Fig. 2 support that the nanoparticle array with strong disorder in the potential wells of ErAs nanoparticles is an Anderson insulator because all states around the Fermi energy are localized [32,43,44].

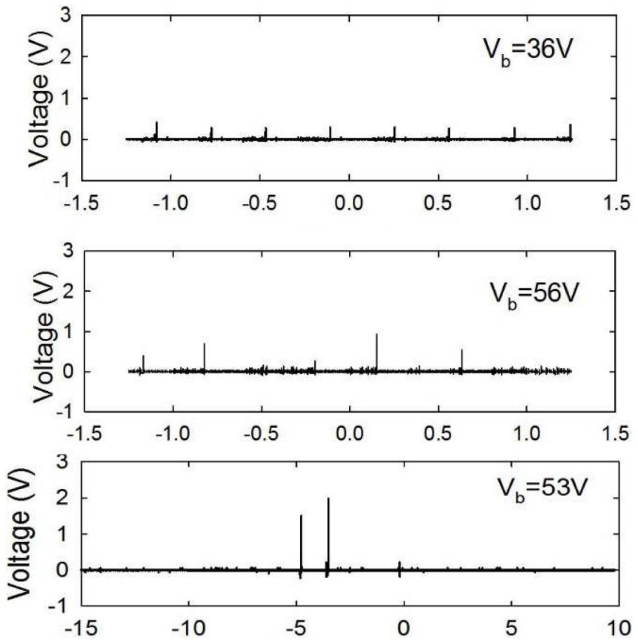

(a)

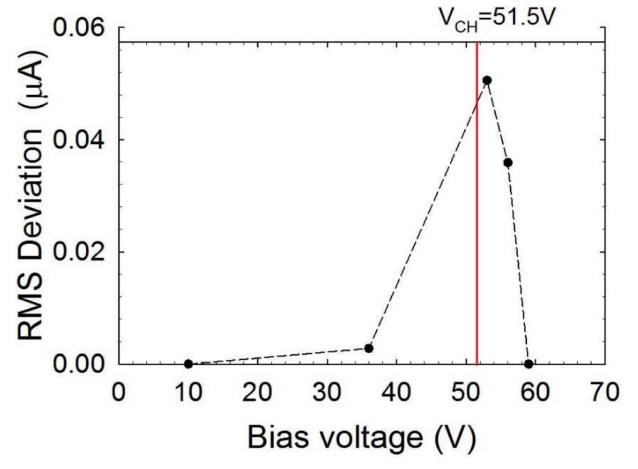

(b)

FIG. 10. (a) Time series of voltage fluctuation at $T = 4.3$ K. (b) rms current fluctuation versus bias voltage.

B. The metallic phase

Whether a material is metal or insulator is determined by the behavior of its conductance with respect to temperature when the temperature approaches absolute zero (Fig. 1 of Ref. [34]). In the insulating regime, the zero-temperature conductivity vanishes. In the metallic regime, the zero-temperature conductivity remains finite. The profound physics underneath is the Ioffe-Regel criterion, $k_F l \sim 1$, where k_F is the Fermi wave number, and l is the mean free path [45]. The metallic regime corresponds to $k_F l \gg 1$ whereas the insulating regime corresponds to $k_F l \ll 1$. For the metallic regime with $k_F l > 1$, the conductance increases as the temperature is lowered.

Figures 8(b) and 11(b) indicate that the samples become metallic at low temperatures. The conductance can be written in the form of $G(T) = G_0 + F(T)$ [34]. The linear fitting of the temperatures $T < 16$ K in Fig. 8(b) yields $G(T) = 2 \times 10^{-7} - 3 \times 10^{-9} T$. $G_0 = 2 \times 10^{-7}$ is likely determined by the extent of disorder [34]. The negative coefficient of $F(T) = -3 \times 10^{-9} T$ shows that the conductance increases while the temperature is lowered. Thus, despite the strong disorder, the conductance at low temperature displays the characteristic metallic behavior $k_F l > 1$.

In Fig. 8(b), we measured an asymptotic current of $\sim$7.0 μA at a bias voltage of 45 V, or a conductance of $G = 1.56 \times 10^{-7}$ S. Given the contact separation of $s = 0.5$ mm and width of $w = 4.5$ mm, and the epitaxial thickness of $t = 1.0$ μm, this corresponds to a bulk electrical conductivity of $g = Gs/A = Gs/(wt) = 1.73 \times 10^{-2}$ S/m. Now we consider the minimum metallic conductivity $\sigma_{\min}$ using the Mott-Ioffe-Regel limit, $\sigma_{\min} = Ce^2/\hbar l$, where e is the electron charge and C is a constant $\approx$0.03 [15,30]. l has a different meaning for different conduction regimes [46]. Here, we

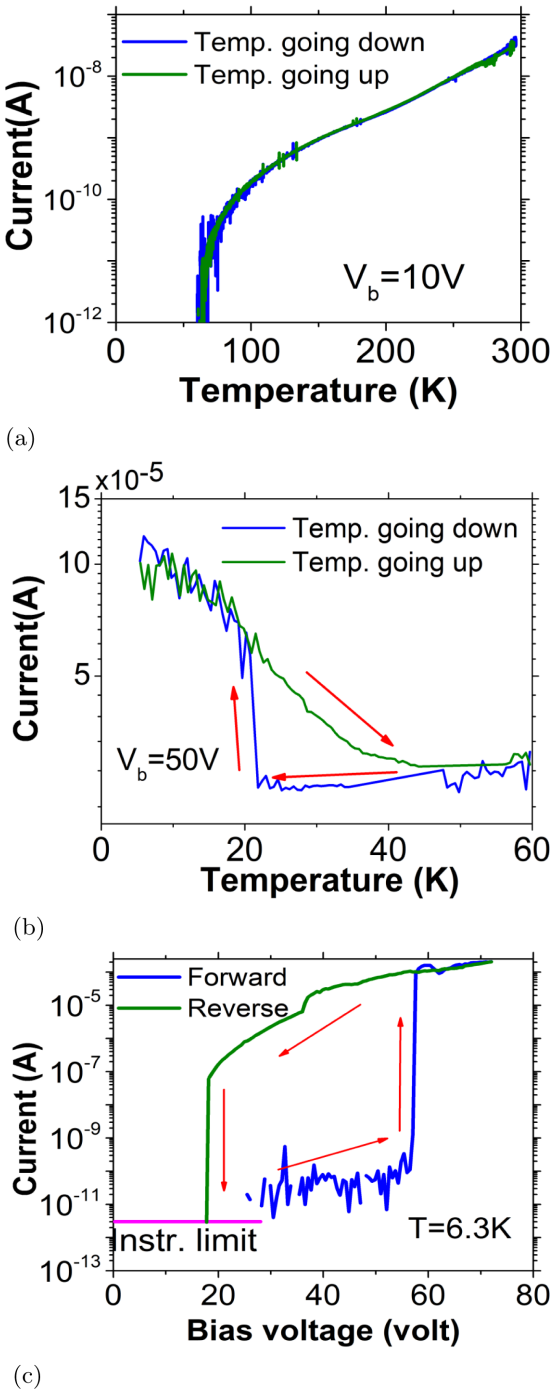

FIG. 11. I vs T behavior for device B2 (structure B). (a) Current vs temperature curve, $V_b = 10$ V. (b) Current vs temperature curve, $V_b = 50$ V. (c) Voltage vs current at a fixed temperature $T = 6.3$ K.

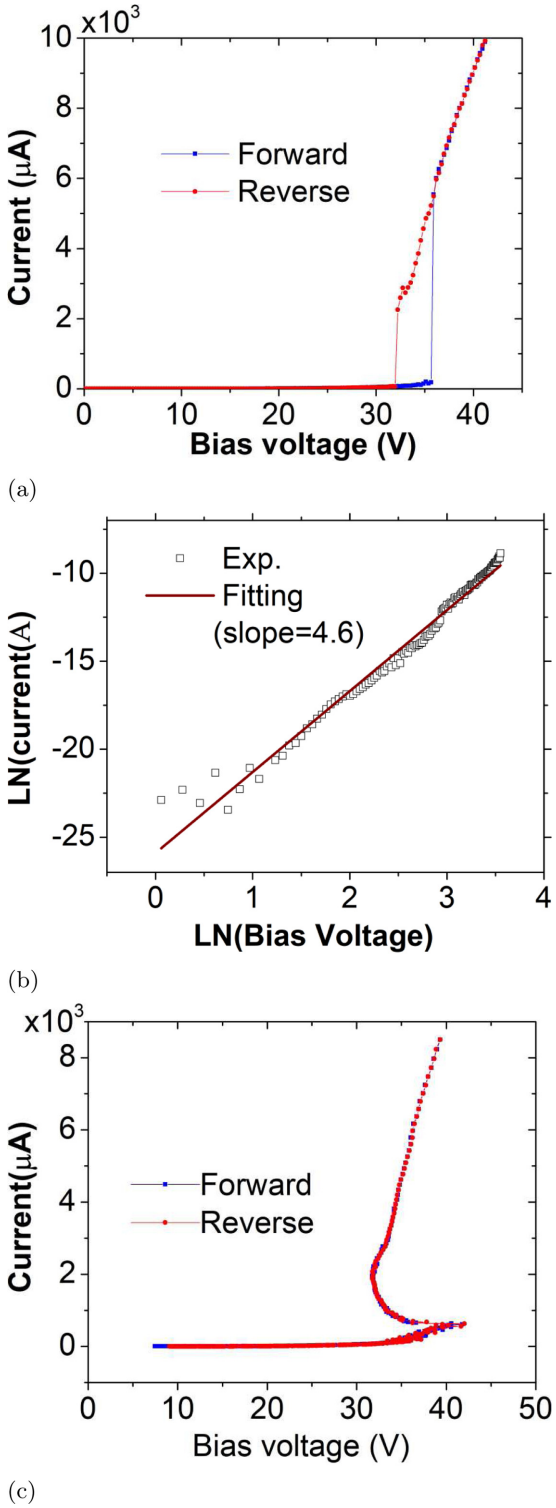

FIG. 12. (a) Voltage-controlled sweeps in both forward and reverse directions for device B3 of structure B. The temperature was $T = 77$ K. (b) The fitting of ln(current) vs ln(voltage) prior to the jump (Table IV). It displays a superlinear relationship between the current and the voltage. (c) Current-controlled sweeps in both forward and reverse directions.

assume l would be the mean separation between nanoparticles assuming they lie so deeply in the GaAs band gap that the only likely transport mechanism is electron hopping. We can estimate l knowing that the Er fraction is 4.0% by volume, and assuming that all nanoparticles have the most likely diameter of 2.5 nm. The resulting l is 5.9 nm, which leads directly to $\sigma_{\min} = 1.24 \times 10^3$ S/m.

Why is the conductivity ($g = 1.73 \times 10^{-2}$ S/m) lower than the minimum metallic conductivity despite that the nanoparticle array displays metallic behavior at low temperatures? According to the analysis in Ref. [19], the pattern of current flow in an array of quantum dots/nanoparticles is through

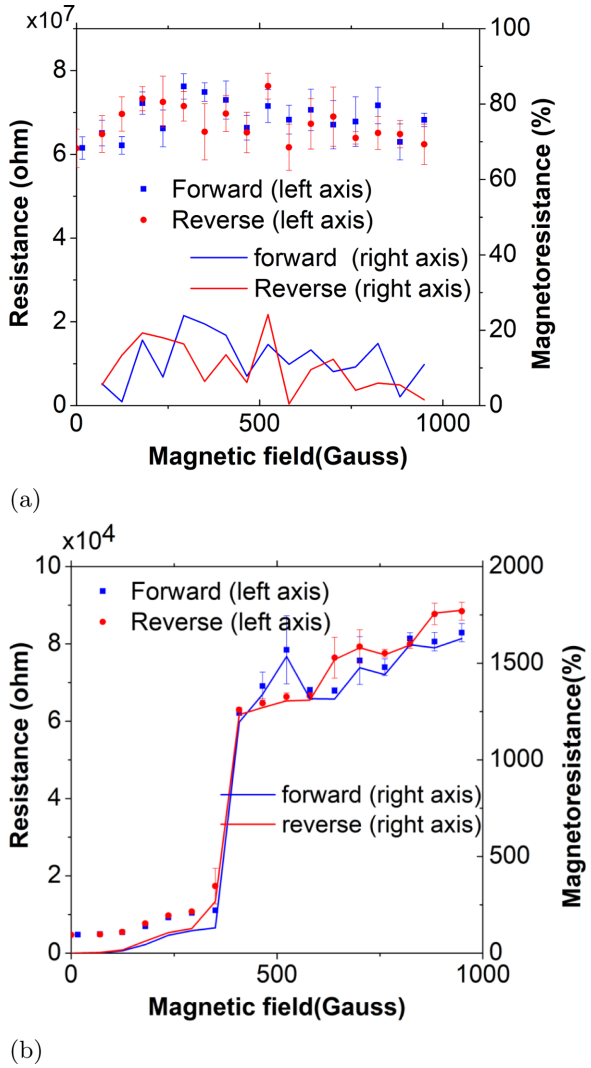

FIG. 13. Device B3. (a) Magnetic field sweeps in both forward and reverse directions; the temperature was $T = 77$ K and the bias was $V_b = 10$ V. (b) Magnetic field sweeps in both forward and reverse directions, $T = 77$ K and $V_b = 39$ V.

multiple paths (or channels) between the two electrodes. However, many paths from the left electrode to the right electrode are still closed, contributing little to the conduction because of the discrete nature of nanoparticles and the nonuniformity of the array. Thus the effective area A' used in the conductivity calculation $g = Gs/A$ contributed by these conducting paths may be much smaller than the area A defined by the geometry of the DUT (e.g., the separation s, the width w, and the thickness t), $A' < A$; the real conductivity g' should be significantly greater than the experimental value g.

In the metallic phase of the nanoparticle array under high bias, the conductance on the temperature-decreasing locus reaches a minimum and tends to increase as the temperature T approaches zero, obeying neither the Arrhenius law or the variable range hopping laws [Fig. 7(b)]. This conductance minimum is strikingly similar to the Kondo effect that occurs to conductance minimum associated with single nonmagnetic quantum dot at low temperature <1 K [47–54].

It is well known that metals with (point) magnetic impurities manifest a resistance minimum due to the Kondo effect when the temperature drops below the Kondo temperature [55–60]. For the scenario of a quantum dot, it is the conductance that displays a minimum because of Kondo resonant scattering by an unpaired spin occupying a bound level of the quantum dot. The underlying Kondo physics for both metal and quantum dots is essentially the same.

The increase in Fig. 8(b) is discontinuous, whereas the single quantum-dot logarithmic behavior is continuous. For the temperature-increasing locus of Fig. 8(a), the discontinuity at the critical temperature is not as steep as for the temperature-decreasing locus of Fig. 8(a), and is found to have a $|\ln(T/T_K)|$ dependence near T_K [Fig. 8(c), Table III], which is a characteristic feature of the Kondo effect [47–54].

How is the localization of the disorder created by the randomness of ErAs nanoparticles weakened? Atomic Er is known to incorporate into the rocksalt crystal structure of ErAs nanoparticles as a trivalent ion Er^{3+} with atomic configuration $4f^{11}$ [61] and an effective magnetic moment of $\sim$5.3 bohr magnetons [9]. An ErAs nanoparticle having the size of those in our samples ($\sim$2.0, nm diameter) can be modeled as an electron potential well containing multiple localized spins of Er ions. As T is lowered below the Kondo temperature, an incident hopping electron may be scattered by the localized spins of the nanoparticle through a spin-flip exchange, which substantially enhances the tunneling probability through the potential well presented by the nanoparticle. Thus, the localization length is enhanced by the presence of Kondo impurities. This agrees with the theory that the transmission of electrons through a barrier can be increased by the presence of magnetic impurities within the barrier [62,63]. Such magnetic-impurity-induced transparency contributed by Kondo resonant transport was confirmed by the experimental studies on a single quantum dot [47–54].

The Kondo spin-flip exchange significantly modifies the energy spectrum of the nanoparticle by creating a sharp resonant state, which is always aligned with the (local) Fermi energy [52]. When Kondo resonance happens collectively in an array of ErAs nanoparticles, the bandwidth W of the density of states (DOS) for the array is reduced but the peak of the DOS grows substantially. Hence, we propose it is the Kondo resonance of the nanoparticle that overcomes the Anderson localization and drives the metal-to-insulator phase transition reported above.

More rigorous theoretical studies by Kettemann [64,65] on 2D Anderson insulators with Kondo impurities predicted that a metal phase is possible in Anderson insulators, supporting our hypothesis above. The theories also predicted a giant magnetoresistance when the density of magnetic impurities is greater than a threshold and the Kondo effect takes place. This agrees with our observation that the metal-to-insulator transition occurs only in the samples with high Er concentration (i.e., the B samples), and the CMR occurs to the metallic phase in weak magnetic fields.

The giant magnetoresistance can be understood from the resistance of the Anderson insulator, which is described in the form of Efros-Shklovskii VRH, $R_{ES} \propto \exp[(T_{es}/T)^{1/2}]$, where $T_{es} = e^2/\epsilon\xi k_B$. k_B is the Boltzmann constant, ϵ is the dielectric constant, and ξ is the localization length [31,46].

ξ is enhanced by magnetic impurities when their density is greater than a threshold [65], leading to metallic phase. When the Zeeman splitting from magnetic field suppresses the Kondo scattering induced correlation, a slight change in the localization length ξ may cause an exponential variation of resistance (or conductance).

Why does the metal-to-insulator transition have a critical dependence on bias voltage? There are two possible reasons. One is that electrons need to overcome the disorder of nanoparticles or quantum dots [19]. This is evidenced by the threshold V_C in the power law $\approx(V_b - V_C)^k$ prior to the current discontinuities [32]. The other is that electrons need to hop far enough from their residential nanoparticle to reach the proximity of its neighboring nanoparticles. It is well known the hopping probability is enhanced by electric field F through a factor of $\sim \exp(eFR_d/2k_BT)$ [30], where R_d is the nearest neighbor distance.

One may argue that the I-V curve in the V mode of Fig. 9(a) is similar to those of n-type GaAs measured at liquid helium temperatures, which previously was explained with impact ionization of shallow neutral donors [66–68]. Despite the similarity, several aspects of our data cannot be explained by the impact ionization effect.

First, in Fig. 8(b) at 45 V bias, as the temperature decreases to 16.3 K, the conductance of device B1 increases abruptly instead of dropping monotonically, as the n-type GaAs does because of the freeze-out of free carriers onto shallow impurities [66]. Second, in our measurements of critical point fluctuations, the rms deviation decays with bias away from the critical point [Fig. 10(b)]. This is contrary to the bias dependence of impact ionization, where the fluctuation generally increases in magnitude above the critical breakdown voltage. Third, the colossal magnetoresistance in Figs. 13(a) and 13(b) occurring only in the metal phase above a threshold bias is very different from the magnetoresistances observed for both pre- and post-impact ionization breakdowns, where the changes were continuous and substantial [69,70].

We also mention that a current discontinuity versus voltage and temperature was reported in p-type GaAs layers doped with Mn, a paramagnetic transition metal. This was explained as a "hole-driven" Mott metal-to-insulator transition model [71]. The physics underlying this effect is different from those of our epitaxial structures, since at the low doping density of Mn used, any nanoparticle formation should not be likely.

IV. CONCLUSION

We have presented a new type of MIT phase transition discovered in GaAs epitaxial structures embedded with ErAs nanoparticles because of high Er concentrations. Transport at lower biases can be well described by the ES VRH among localized states. And the conductance disappears as the temperature drops toward absolute zero. Because the insulating phase is traced to the disorder of the nanoparticle potentials, it is categorized as an Anderson insulator. The transport at high biases displays a conductance minimum, a drastic increase in conductance at lower temperatures, and then a finite zero-temperature conductance, accompanied by hysteretic behaviors and great magnetoresistances. This metallic phase is likely related to a cooperative behavior among the nanoparticles via Kondo scattering. Thus, we argue that the voltage-controlled MIT may be explained with the conduction mechanisms of an Anderson insulator with Kondo impurities.

ACKNOWLEDGMENTS

This material is based on work supported by or in part by the U.S. Army Research Laboratory and the U.S. Army Research Office under Contract No. W911NF-12-1-0496 and Contract No. W911NF19C0044 (program manager Joe Qiu). Contributions to this article by workers at NIST, an agency of the U.S. Government, are not subject to U.S. copyright.

[1] S. Gupta, S. Sethi, and P. K. Bhattacharya, Picosecond carrier lifetime in erbium-doped-GaAs, Appl. Phys. Lett. **62**, 1128 (1993).

[2] S. Sethi and P. K. Bhattacharya, Characteristics and device applications of erbium doped III-V semiconductors grown by molecular beam epitaxy, J. Electron. Mater. **25**, 467 (1996).

[3] C. Kadow, A. W. Jackson, A. C. Gossard, S. Matsuura, and G. A. Blake, Self-assembled ErAs islands in GaAs for optical heterodyne THz generation, Appl. Phys. Lett. **76**, 3510 (2000).

[4] M. Griebel, J. H. Smet, D. C. Driscoll, J. Kuhl, C. A. Diez, N. Freytag, C. Kadow, A. C. Gossard, and K. von Klitzing, Tunable subpicosecond optoelectronic transduction in superlattices of self-assembled ErAs nanoislands, Nat. Mater. **2**, 122 (2003).

[5] I. Poole, K. E. Singer, A. R. Peaker, and A. C. Wright, Growth and structural characterization of molecular beam epitaxial erbium-doped GaAs, J. Cryst. Growth **121**, 121 (1992).

[6] J. M. Zide, D. O. Klenov, S. Stemmer, A. C. Gossard, G. Zeng, J. E. Bowers, D. Vashaee, and A. Shakouri, Thermoelectric power factor in semiconductors with buried epitaxial semimetallic nanoparticles, Appl. Phys. Lett. **87**, 112102 (2005).

[7] C. J. Palmstrøm, N. Tabatabaie, and S. J. Allen, Epitaxial growth of ErAs on (100) GaAs, Appl. Phys. Lett. **53**, 2608 (1988).

[8] J. Zimmerman, E. R. Brown, and A. C. Gossard, Tunable all epitaxial semimetal-semiconductor Schottky diode system: ErAs on InAlGaAs, J. Vac. Sci. Technol. B **23**, 1929 (2005).

[9] S. J. Allen, N. Tabatabaie, C. J. Palmstrøm, G. W. Hull, T. Sands, F. DeRosa, H. L. Gilchrist, and K. C. Garrison, ErAs Epitaxial Layers Buried in GaAs: Magnetotransport and Spin-Disorder Scattering, Phys. Rev. Lett. **62**, 2309 (1989).

[10] E. R. Brown, A. Bacher, D. Driscoll, M. Hanson, C. Kadow, and A. C. Gossard, Evidence for a Strong Surface-Plasmon Resonance on ErAs Nanoparticles in GaAs, Phys. Rev. Lett. **90**, 077403 (2003).

[11] J. Middendorf and E. Brown, ErAs:GaAs THz pulse generation using extrinsic photoconductivity at 1550 nm, Opt. Express **20**, 16504 (2012).

[12] A. Mingardi, W.-D. Zhang, E. R. Brown, A. D. Feldman, T. E. Harvey, and R. P. Mirin, High power generation of THz from 1550-nm photoconductive emitters, Opt. Express **26**, 14472 (2018).

[13] W.-D. Zhang, E. R. Brown, A. Mingardi, R. P. Mirin, N. Jahed, and D. Saeedkia, THz superradiance from a GaAs:ErAs quantum dot array at room temperature, Appl. Sci. **9**, 3014 (2019).

[14] T. F. Rosenbaum, R. F. Milligan, M. A. Paalanen, G. A. Thomas, R. N. Bhatt, and W. Lin, Metal-insulator transition in a doped semiconductor, Phys. Rev. B **27**, 7509 (1983).

[15] N. Mott, The mobility edge since 1967, J. Phys. C: Solid State Phys. **20**, 3075 (1987).

[16] L. J. Geerligs, D. V. Averin, and J. E. Mooij, Observation of Macroscopic Quantum Tunneling through the Coulomb Energy Barrier, Phys. Rev. Lett. **65**, 3037 (1990).

[17] Y. Hirano, Y. Segawa, F. Yamada, T. Kuroda-Sowa, T. Kawai, and T. Matsumoto, Mn_{12} molecular redox array exhibiting one-dimensional Coulomb blockade behavior, J. Phys. Chem. C **116**, 9895 (2012).

[18] A. Zabet-Khosousi, P. E. Trudeau, Y. Suganuma, A. A. Dhirani, and B. Statt, Metal to Insulator Transition in Films of Molecularly Linked Gold Nanoparticles, Phys. Rev. Lett. **96**, 156403 (2006).

[19] A. A. Middleton and N. S. Wingreen, Collective Transport in Arrays of Small Metallic Dots, Phys. Rev. Lett. **71**, 3198 (1993).

[20] G. Landwehr and W. Ossau, editors, Universal conductance fluctuations and telegraph noise spectroscopy to investigate the magnetisation of self-organized ErAs quantum frequencies, in *High Magnetic Fields in the Physics of Semiconductors: Proceedings of the 12th International Conference* (World Scientific, Würzburg, Germany, 1997).

[21] D. R. Schmidt, A. G. Petukhov, M. Foygel, J. P. Ibbetson, and S. J. Allen, Fluctuation Controlled Hopping of Bound Magnetic Polarons in ErAs:GaAs Nanocomposites, Phys. Rev. Lett. **82**, 823 (1999).

[22] K. M. Hanif, R. W. Meulenberg, and G. F. Strouse, Magnetic ordering in doped $Cd_{1-x}Co_xSe$ diluted magnetic quantum dots, J. Am. Chem. Soc. **124**, 11495 (2002).

[23] M. Holub, S. Chakrabarti, S. Fathpour, P. Bhattacharya, Y. Lei, and S. Ghosh, Mn-doped InAs self-organized diluted magnetic quantum-dot layers with Curie temperatures above 300 K, Appl. Phys. Lett. **85**, 973 (2004).

[24] F.-X. Xiu, Y. Wang, J.-Y. Kim, A. Hong, J.-S. Tang, A. P. Jacob, J. Zou, and K.-L. Wang, Electric-field-controlled ferromagnetism in high-Curie-temperature $Mn_{0.05}Ge_{0.95}$ quantum dots, Nat. Mater. **9**, 337 (2010).

[25] J. M. Pientka, R. Oszwaldowski, A. G. Petukhov, J. E. Han, and I. Žutić, Magnetic ordering in quantum dots: Open versus closed shells, Phys. Rev. B **92**, 155402 (2015).

[26] E. R. Brown, A. Mingardi, W.-D. Zhang, A. D. Feldman, T. E. Harvey, and R. P. Mirin, Abrupt dependence of ultrafast extrinsic photoconductivity on Er fraction in GaAs:Er, Appl. Phys. Lett. **111**, 031104 (2017).

[27] See Supplemental Material at http://link.aps.org/supplemental/10.1103/PhysRevResearch.4.043040 for more information.

[28] M. A. Scarpulla, J. M. O. Zide, J. M. LeBeau, C. G. V. de Walle, A. C. Gossard, and K. T. Delaney, Near-infrared absorption and semimetal-semiconductor transition in 2 nm ErAs nanoparticles embedded in GaAs and AlAs, Appl. Phys. Lett. **92**, 173116 (2008).

[29] J. K. Kawasaki, R. Timm, K. T. Delaney, E. Lundgren, A. Mikkelsen, and C. J. Palmstrøm, Local Density of States and Interface Effects in Semimetallic ErAs Nanoparticles Embedded in GaAs, Phys. Rev. Lett. **107**, 036806 (2011).

[30] N. F. Mott, *Conduction in Non-Crystalline Materials* (Clarendon Press, Oxford, 1993).

[31] B. I. Shklovskii and A. L. Efros, *Electronic Properties of Doped Semiconductors* (Springer, Verlag Berlin Heidelberg, 1984).

[32] T. B. Tran, I. S. Beloborodov, X. M. Lin, T. P. Bigioni, V. M. Vinokur, and H. M. Jaeger, Multiple Cotunneling in Large Quantum Dot Arrays, Phys. Rev. Lett. **95**, 076806 (2005).

[33] A. L. Efros and B. I. Shklovskii, Coulomb gap and low temperature conductivity of disordered systems, J. Phys. C: Solid State Phys. **8**, L49 (1975).

[34] A. J. Heeger, The critical regime of the metal-insulator transition in conducting polymers: Experimental studies, Phys. Scr., T **102**, 30 (2002).

[35] H. E. Stanley, *Introduction to Phase Transitions and Critical Phenomena* (Oxford University Press, New York Oxford, 1971).

[36] F. Jegerlehner, *Critical Phenomena and the Renormalization Group*, Lecture in Troisième Cycle de la Physique en Suisse Romande (Universität Bielefeld, Bielefeld, 1976).

[37] M. A. Anisimov, Letter to the editor: Fifty years of breakthrough discoveries in fluid criticality, Int. J. Thermophys. **32**, 2001 (2011).

[38] M. R. Oliver, J. O. Dimmock, A. L. McWhorter, and T. B. Reed, Conductivity studies in europium oxide, Phys. Rev. B **5**, 1078 (1972).

[39] V. Podzorov, M. Uehara, M. E. Gershenson, T. Y. Koo, and S.-W. Cheong, Giant $1/f$ noise in perovskite manganites: Evidence of the percolation threshold, Phys. Rev. B **61**, R3784 (2000).

[40] V. Podzorov, M. E. Gershenson, M. Uehara, and S.-W. Cheong, Phase separation and $1/f$ noise in low-T_{MI} colossal magnetoresistance manganites, Phys. Rev. B **64**, 115113 (2001).

[41] V. Podzorov, B. G. Kim, V. Kiryukhin, M. E. Gershenson, and S.-W. Cheong, Martensitic accommodation strain and the metal-insulator transition in manganites, Phys. Rev. B **64**, 140406(R) (2001).

[42] Y. Tokura, Correlated electrons: Science to technology, JSAP Int. **2000**(2), 12 (2000).

[43] P. W. Anderson, Absence of diffusion in certain random lattices, Phys. Rev. **109**, 1492 (1958).

[44] E. Abrahams, P. W. Anderson, D. C. Licciardello, and T. V. Ramakrishnan, Scaling Theory of Localization: Absence of Quantum Diffusion in Two Dimensions, Phys. Rev. Lett. **42**, 673 (1979).

[45] A. Ioffe and A. Regel, Non-crystalline, amorphous and liquid electronic semiconductors, Prog. Semicond. **4**, 237 (1960).

[46] A. Zabrodskiĭ and K. Zinov'eva, Low-temperature conductivity and metal-insulator transition in compensate *n*-Ge, Zh. Eksp. Teor. Fiz. **86**, 727 (1984).

[47] D. Goldhaber-Gordon, H. Shtrikman, D. Mahalu, D. Abusch-Magder, U. Meirav, and M. A. Kastner, Kondo effect in a single electron transistor, Nature (London) **391**, 156 (1998).

[48] S. M. Cronenwett, T. H. Oosterkamp, and K. P. Kouwenhoven, Tunable Kondo effect in quantum dots, Science **281**, 540 (1998).

[49] F. Simmel, R. H. Blick, J. P. Kotthaus, W. Wegscheider, and M. Bichler, Anomalous Kondo Effect in a Quantum Dot at Nonzero Bias, Phys. Rev. Lett. **83**, 804 (1999).

[50] S. Sasaki, S. D. Franceschi, J. M. Elzerman, W. G. V. der Wiel, M. Eto, S. Tarucha, and L. P. Kouwenhoven, Kondo effect in an integer-spin quantum dot, Nature (London) **405**, 764 (2000).

[51] R. M. Potok, I. G. Rau, H. Shtrikman, Y. Oreg, and D. Goldhaber-Gordon, Observation of the two channel Kondo effect, Nature (London) **446**, 167 (2007).

[52] L. Kouwenhoven and L. Glazman, Revival of the Kondo effect, Phys. World **14**, 33 (2001).

[53] M. Pustilnik and L. I. Glazman, Kondo effect in quantum dots, J. Phys.: Condens. Matter **16**, R513 (2004).

[54] M. Grobis, I. G. Rau, R. M. Potok, and D. Goldhaber-Gordon, The Kondo effect in mesoscopic quantum dots, in *Handbook of Magnetism and Advanced Magnetic Materials* (John Wiley and Sons, 2007).

[55] J. Kondo, Resistance minimum in dilute magnetic alloys, Prog. Theor. Phys. **32**, 37 (1964).

[56] A. A. Abrikosov, Electron scattering on magnetic impurities in metals and anomalous resistivity effects, Phys. Phys. Fiz. **2**, 5 (1965).

[57] H. Suhl, Dispersion theory of the Kondo effect, Phys. Rev. **138**, A515 (1965).

[58] Y. Nagaoka, Self-consistent treatment of Kondo's effect in dilute alloys, Phys. Rev. **138**, A1112 (1965).

[59] P. W. Anderson, Localized magnetic states in metals, Phys. Rev. **124**, 41 (1961).

[60] P. W. Anderson, A poor man's derivation of scaling laws for the Kondo problem, J. Phys. C: Solid State Phys. **3**, 2436 (1970).

[61] T. Komesu, H.-K. Jeong, J. Choi, C. N. Borca, P. A. Dowben, A. G. Petukhov, B. D. Schultz, and C. J. Palmstrøm, Electronic structure of ErAs (100), Phys. Rev. B **67**, 035104 (2003).

[62] T.-K. Ng and P. A. Lee, On-Site Coulomb Repulsion and Resonant Tunneling, Phys. Rev. Lett. **61**, 1768 (1988).

[63] L. I. Glazman and M. E. Raikh, Resonant Kondo transparency of a barrier with quasilocal impurity states, JETP Lett. **47**, 452 (1988).

[64] S. Kettemann, E. R. Mucciolo, and I. Varga, Critical Metal Phase at the Anderson Metal-Insulator Transition with Kondo Impurities, Phys. Rev. Lett. **103**, 126401 (2009).

[65] S. S. Kettemann and M. E. Raikh, Localization Length in Anderson Insulator with Kondo Impurities, Phys. Rev. Lett. **90**, 146601 (2003).

[66] D. J. Oliver, Electrical properties of *n*-type gallium arsenide, Phys. Rev. **127**, 1045 (1962).

[67] E. Schöll, Bistability and nonequilibrium phase transitions in a semiconductor recombination model with impact ionization of donors, Z. Phys. B **46**, 23 (1982).

[68] F. Karel, J. Oswald, J. Pastrňák, and Peteříček, Impurity breakdown and electric-field-dependent luminescence in MBE and VPE GaAs layers, Semicond. Sci. Technol. **7**, 203 (1992).

[69] K. Aoki, T. Kondo, and T. Watanabe, Cross-over instability and chaos of hysteretic I-V curve during impurity avalanche breakdown in n-GaAs under longitudinal magnetic field, Solid State Commun. **77**, 91 (1991).

[70] V. A. Samuilov, V. K. Ksenevich, G. Remenyi, G. Kiss, and B. Podor, Impact ionization breakdown of n-GaAs in high magnetic fields, Semicond. Sci. Technol. **14**, 1084 (1999).

[71] S. Choi, B.-J. Kim, Y.-W. Lee, Y.-S. Lim, J. Choi, and H.-T. Kim, Control of current-jump induced by voltage, temperature, light in p-type GaAs: Programmable critical temperature sensor, Appl. Phys. Lett. **95**, 231910 (2009).